JGR Atmospheres

RESEARCH ARTICLE
10.1029/2019JD031599

Zonal Wave Number Diagnosis of Rossby Wave-Like Oscillations Using Paired Ground-Based Radars

Maosheng He[1], Yosuke Yamazaki[2], Peter Hoffmann[1], Chris M. Hall[3], Masaki Tsutsumi[4], Guozhu Li[5], and Jorge Luis Chau[1]

[1]Leibniz-Institute of Atmospheric Physics at the Rostock University, Kühlungsborn, Germany, [2]GFZ German Research Centre for Geosciences, Potsdam, Germany, [3]Tromsø Geophysical Observatory, UiT-The Arctic University of Norway, Tromsø, Norway, [4]National Institute of Polar Research, Tokyo, Japan, [5]Beijing National Observatory of Space Environment, Institute of Geology and Geophysics, Chinese Academy of Sciences, Beijing, China

Key Points:

- Two radars at polar latitude are combined to diagnose zonal wave number m of Rossby wave-like oscillations occurring around four SSW onsets
- Transient 10- and 16-day oscillations are mostly associated with $m = 1$, and therefore should be Rossby wave normal modes
- A 16-day oscillation is associated with $m = 2$, resulting potentially from nonlinear interactions of the 16-day wave with a stationary Rossby wave

Correspondence to:
M. He,
he@iap-kborn.de

Citation:
He, M., Yamazaki, Y., Hoffmann, P., Hall, C. M., Tsutsumi, M., Li, G., & Chau, J. L. (2020). Zonal wave number diagnosis of Rossby wave-like oscillations using paired ground-based radars. *Journal of Geophysical Research: Atmospheres*, *125*, e2019JD031599. https://doi.org/10.1029/2019JD031599

Received 19 SEP 2019
Accepted 29 APR 2020
Accepted article online 3 MAY 2020

Abstract Free traveling Rossby wave normal modes (RNMs) are often investigated through large-scale space-time spectral analyses, which therefore is subject to observational availability, especially in the mesosphere. Ground-based mesospheric observations were broadly used to identify RNMs mostly according to the periods of RNMs without resolving their horizontal scales. The current study diagnoses zonal wave numbers of RNM-like oscillations occurring in mesospheric winds observed by two meteor radars at about 79°N. We explore four winters comprising the major stratospheric sudden warming events (SSWs) 2009, 2010, and 2013. Diagnosed are predominant oscillations at the periods of 10 and 16 days lasting mostly for three to five whole cycles. All dominant oscillations are associated with westward zonal wave number $m = 1$, excepting one 16-day oscillation associated with $m = 2$. We discuss the $m = 1$ oscillations as transient RNMs and the $m = 2$ oscillation as a secondary wave of nonlinear interaction between an RNM and a stationary Rossby wave. All the oscillations occur around onsets of the three SSWs, suggesting associations between RNMs and SSWs. For comparison, we also explore the wind collected by a similar network at 54°N during 2012–2016. Explored is a manifestation of 5-day wave, namely, an oscillation at 5–7 days with $m = 1$), around the onset of SSW 2013, supporting the associations between RNMs and SSWs.

Plain Language Summary Most detectable atmospheric Rossby waves are associated with atmospheric intrinsic properties, including the free traveling Rossby wave normal modes and forced resonant stationary Rossby waves. The former is less understood than the latter because they are relatively weak and often distorted by the background atmosphere. In the current work, we customize a compact wave identifying technique to estimate the horizontal wavelength of Rossby wave-like predominant 10- and 16-day oscillations detected by two arctic radars during stratospheric sudden warming events. Results illustrate that five of the six most oscillations are westward traveling with zonal wave number 1. We explain the oscillations as free transient Rossby wave normal modes.

1. Introduction

Rossby waves (RWs) were identified initially by Rossby (1939) as solutions of simplified terrestrial atmospheric dynamic equations constrained by the conservation of potential vorticity. RWs are horizontal transverse waves whose restoring mechanism is provided by the meridian gradient of the Coriolis force, namely, the beta effect (e.g., Holton & Hakim, 2013). The restoring mechanism resists meridional displacements and drives the waves propagating zonally. Since the beta effect occurs in all types of rotating fluid, RWs could also be produced in laboratory experiments (e.g., Tajima & Nakamura, 2005) and also develop naturally in various astronomical objects, for example, planetary atmospheres and oceans (e.g., Allison, 1990; Read et al., 2009), plasma on the Sun (McIntosh et al., 2017), and Keplerian disk (Lovelace et al., 1999).

In the terrestrial atmosphere, the most spectacular RWs are associated with the atmospheric intrinsic properties, including the free traveling Rossby wave normal modes (RNMs; e.g., Madden, 1979) and forced resonant stationary Rossby waves (SRWs; e.g., Tung & Lindzen, 1979). RNMs are often referred to with a pair of numbers $(m, n - m)$, which are referring to the associated Legendre function of degree n and order m (e.g., Madden, 1979). The most commonly observed RNMs are those with the longest horizontal

wavelengths, for example, modes (1, 1), (1, 2), (1, 3), which travel westward with periods of 5, 8.3, and 12.5 days, Doppler shifted by the ambient westerly and known as 5-, 10-, and 16-day waves, respectively (e.g., Forbes, 1995a; Forbes & Zhang, 2015; Longuet-Higgins, 1968; Salby, 1984; Weber & Madden, 1993). RNMs could develop in an unbounded or zonally symmetric atmosphere, whereas a zonally asymmetric atmospheric lower boundary due to, for example, topographic or thermal condition gives rise to SRWs, namely, resonant circulations which are stationary relative to the surface of the Earth (Holton & Hakim, 2013). In the frame of reference rotating with the mean flow, SRW is traveling westward with phase velocity at the magnitude of the flow speed of the background westerly. Note that SRW is not a classic stationary wave (also called standing waves coined by Melde, 1860) that does also not travel in space but oscillates in time. The most significant RNMs and SRWs have planetary-scale horizontal wavelengths. Therefore, RWs, RNMs, and SRWs are also called planetary waves, traveling planetary waves, and stationary planetary waves, respectively.

RWs play a significant role in angular momentum processes in the atmosphere and are of most importance for determining large-scale weather phenomena (Smith, 1985). In particular, the large-scale SRWs, excited by the zonal gradient of the land-sea thermal condition in the winter polar region, interact nonlinearly with the mean zonal circulation and generate the most spectacular atmospheric process, namely, the sudden stratospheric warming event (SSW; e.g., Matsuno, 1971; Reed, 1963). While SRWs play a crucial role in initiating SSWs (e.g., Matsuno, 1971), the behavior of RNMs in SSWs is still under debate. The association between RNMs and SSWs is supported by some studies (e.g., Pancheva et al., 2008; Yamazaki & Matthias, 2019), but not by others (e.g., Sassi et al., 2012). The contradiction is, at least partially, due to difficulties in the observational identification of RNMs. The identification is typically not straightforward but entails careful spatial-temporal spectral filtering of measurements covering long distances for a long time. Besides, the identifications are considerably subject to distortions from the background flow and other atmospheric oscillations, for example, tides and gravity waves, which are on shorter temporal and spatial scales with potentially stronger intensities than RWs. These difficulties made the RW be one of the rare atmospheric phenomena which were predicted theoretically before they were discovered observationally.

Early observational evidence of RNM in the troposphere and lower stratosphere was extracted from globally distributed meteorological records (e.g., as reviewed comprehensively in Madden, 1979; Salby, 1984). RNM climatology in the troposphere (Weber & Madden, 1993) and stratosphere (Fedulina et al., 2004) were investigated using European Center for Medium-range Weather Forecasts analyses(ECMWF) model and UK Met Office (UKMO) assimilated data. However, in the mesosphere and low thermosphere (MLT) regions, RNM evidence has been relatively rarely reported. Space-based MLT observations could capture RNM (e.g., McDonald et al., 2011) with constraints of both frequency and wave number but are subject to aliasing associated with the most common slowly precessing polar orbits (e.g., Salby, 1982a, 1982b). Observations collected by ground-based radars provided long records of MLT winds, but they are only available at a limited number of sites. Consequently, radars are typically used to explore RNM through spectrum analysis using single-station techniques without determining horizontal scales. To conquer this problem, the current study adapts a dual-station technique developed recently by He, Chau, Stober, et al. (2018) to diagnose the zonal wave number of RNM signatures using two zonally separated radars. Although the technique was initially developed for diagnosing the wave number of tides, it should be capable of diagnosing RNM signatures given that the zonal scales of tides are comparable to those of RNMs. In the current work, we demonstrate this capability.

According to the classical wave theory (e.g., Figure 2 in Madden, 1982b), RNMs are structural in the meridional direction. For a meridional comparison, we collect two dual-station networks, at middle and high latitudes, respectively. We will check both zonal and meridional wind components as the classical theory predicts that the meridional structures are different between the two components. Below, after introducing the approach and data set in section 2, we display the results in section 3, and explain the results and discuss their implications in section 4.

2. Data Analysis

The current work uses two dual-station networks, as displayed in Figure 1, comprising four specular meteor radars at Svalbard (78°N, 16°E; cf. Hall et al., 2002), Eureka (80°N, 86°W; cf. Manson et al., 2009), Juliusruh (54.6°N, 13.4°E; cf. Singer et al., 2013), and Mohe (53.0°N, 122.5°E; cf. Yu et al., 2013). The networks were used in He, Chau, Hall, et al. (2018) and He, Chau, Stober, et al. (2018), respectively. In the current work, the

Figure 1. Distribution of radars used for the current work, comprising a high-latitude pair at Eureka (80°N, 86°W) and Svalbard(78°N, 16°E), and a midlatitude pair at Juliusruh (54.6°N, 13.4°E) and Mohe (54.0°N, 122.5°E).

main results are based on the polar network, which is complemented by the midlatitude network. Hourly wind observation is available for four winters during 2008–2012 at the polar network (see Figure 2a), and for five years 2012–2016 at the midlatitude network (see Figure 2a).

Ground-based observations were used to investigate RWs typically through single-station analysis approaches and therefore were not capable of diagnosing the horizontal scale. Recently, globally distributed stations were combined to investigate the horizontal structure of RNMs, both the meridional (Jiang et al., 2008) and zonal (Elhawary & Forbes, 2016). Elhawary and Forbes (2016) analyzed data from two stations that are located at the same latitude but are separated in longitude by 180°, to diagnose RNMs with zonal wave number $m = 1$. Other studies used paired stations that are separated in longitude by arbitrary degrees to identify m through analyzing the spectral phase of RNM-like oscillations (Clark et al., 2002; Pancheva et al., 2008; Pogoreltsev et al., 2002) and semidiurnal tides (e.g., Manson et al., 2009; Murphy, 2003). Recently, He, Chau, Stober, et al. (2018) developed a dual-station approach called phase differencing technique (PDT) to estimate the wave number of tides as a spectrum within broad ranges of time t and frequency f. PDT is briefly introduced in Appendix A1. Below we implement PDT to explore RNMs.

3. Results

In the current section, we apply PDT to diagnose m of RNM-like oscillations through wavelet and cross-wavelet analyses using the dual-station networks. The results from the polar network are detailed in sections 3.1–3.4, whereas those from the middle latitudes are concisely present in section 3.5 for comparison.

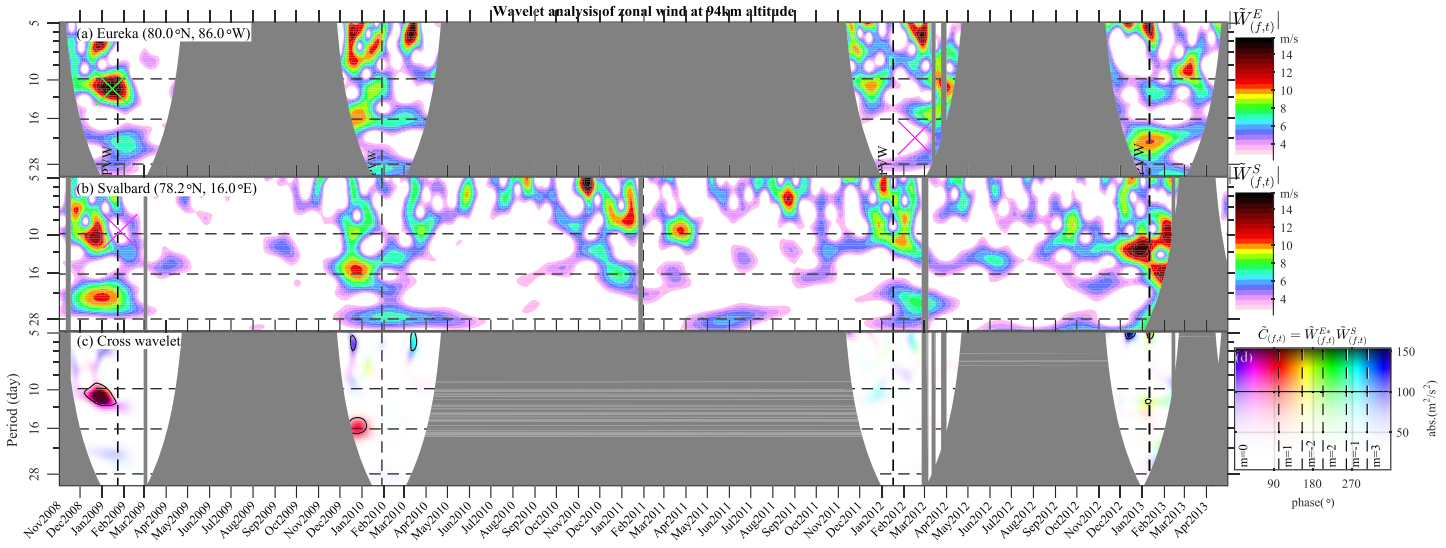

Figure 2. Wavelet spectra $\tilde{W}^E_{(f,t)}$ and $\tilde{W}^S_{(f,t)}$ of the hourly zonal wind at 94 km altitude, observed by specular meteor radars at (a) Eureka (80.0°N, 86.0°W) and (b) Svalbard (78.2°N, 16.0°E), respectively. (c) The cross-wavelet spectrum between (a) and (b): $\tilde{C}_{(f,t)} = \tilde{W}^{E*}_{(f,t)}\tilde{W}^S_{(f,t)}$. In (c), $\tilde{C}_{(f,t)}$ reads referring to (d): the darkness of the map represents its amplitude, whereas the hue of the color represents its phase, and the phase values associated with five zonal wave numbers (m) are displayed by the vertical dashed line. In (d), the vertical dashed lines indicate the phase difference associated with zonally propagating waves with four zonal wave numbers. In (a)–(c), the vertical dashed line represents the polar vortex-weakening central day (PVW). The ticks and labels of the x axis represent the first day of each month. The magenta and green crosses represent the coordinates on which the portions will be compared with the spectra of the meridional component displayed in Figure 4. Shadowed are intervals missing data or influenced by the edge effect of the discontinuity of finite-length time series.

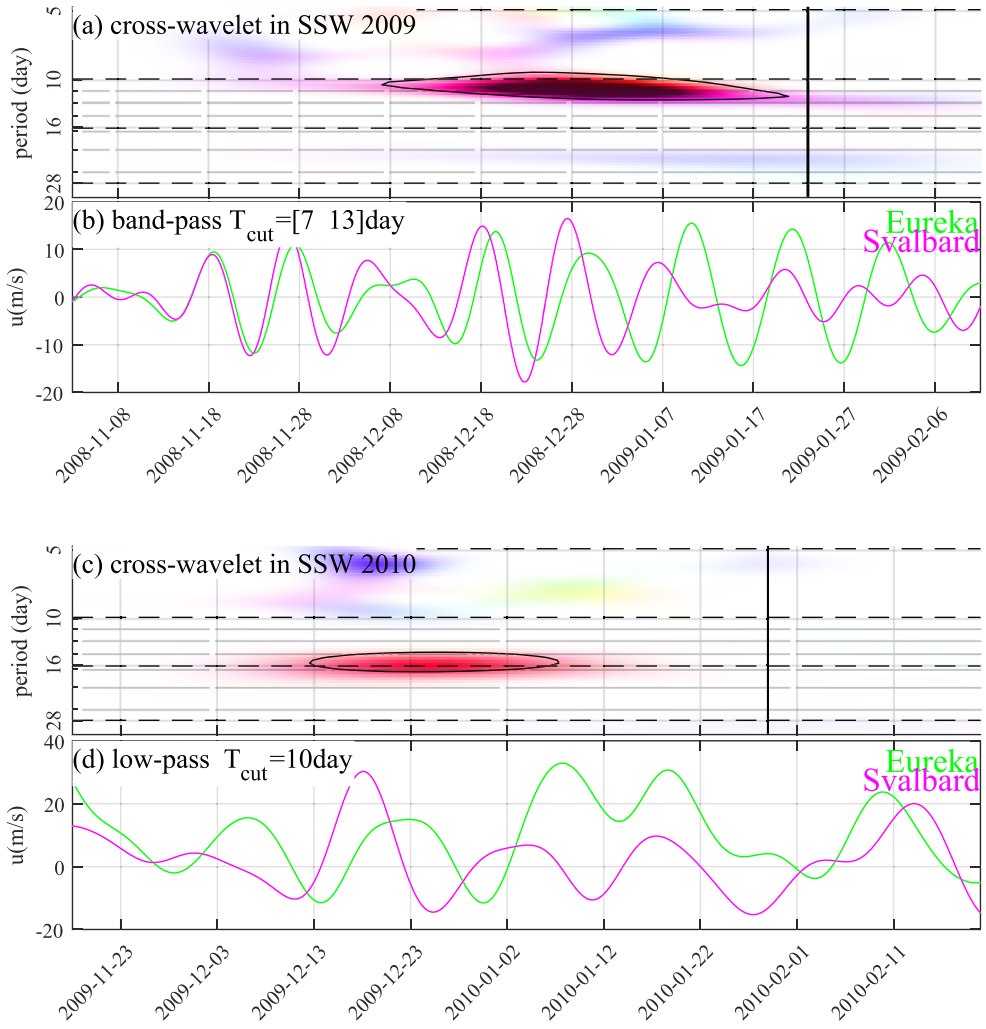

Figure 3. (a) Same plot as Figure 2 zoomed into the period of SSW 2009. (b) Butterworth filtered zonal wind during SSW 2009 at Eureka (magenta, at 80.0°N, 86.0°W) and (b) Svalbard (green, at 78.2°N, 16.0°E). (c, d) Similar plots as (a) and (b) but for SSW 2010.

3.1. Wavelet Spectra of Zonal Wind

Figures 2a and 2b show the wavelet spectra, $\tilde{W}^E_{(f,t)}$ and $\tilde{W}^S_{(f,t)}$, of the hourly zonal wind at 94 km altitude over Eureka and Svalbard between late 2008 and early 2013, which are the estimations of $\tilde{u}(\lambda_1, t)$ and $\tilde{u}(\lambda_2, t)$ in equation (A1), respectively. Used is a Morlet wavelet with factor 8, namely, a mother function composed of a complex exponential carrier tailored by a Gaussian envelope (Grossmann et al., 1990). The spectra are populated with isolated peaks, in both period and time. The isolation in time suggests that the oscillations are transient while the isolated period was often used as evidence of RNWs. The peaks occur both before and after the SSW onsets that are represented by the vertical dashed lines in Figure 2c. The onsets refer to the dates of the polar vortex weakening (PVW Siddiqui et al., 2015; Zhang & Forbes, 2014).

3.2. Cross-Wavelet Spectrum and Wave Number Diagnosis

Figure 2c displays the cross-wavelet spectrum between the spectra in Figures 2a and 2b, $\tilde{C}_{(f,t)} = \tilde{W}^{E*}_{(f,t)}\tilde{W}^S_{(f,t)}$, which corresponds to the estimation $\hat{\tilde{p}}$ in equation (A3). The spectrum is color coded referring to the scheme shown in panel (d) so that the darkness represents the magnitude $|\tilde{C}_{(f,t)}|$, whereas the color hue represents the phase $Arg\{\tilde{C}_{(f,t)}\}$. The amplitude quantifies the intensity of co-occurred oscillations, while the phase measures the phase difference between the radars which further allows estimating the zonal wave number m. In panel (d), the vertical dashed lines represent the phase difference associated with $m \in M_c$ where

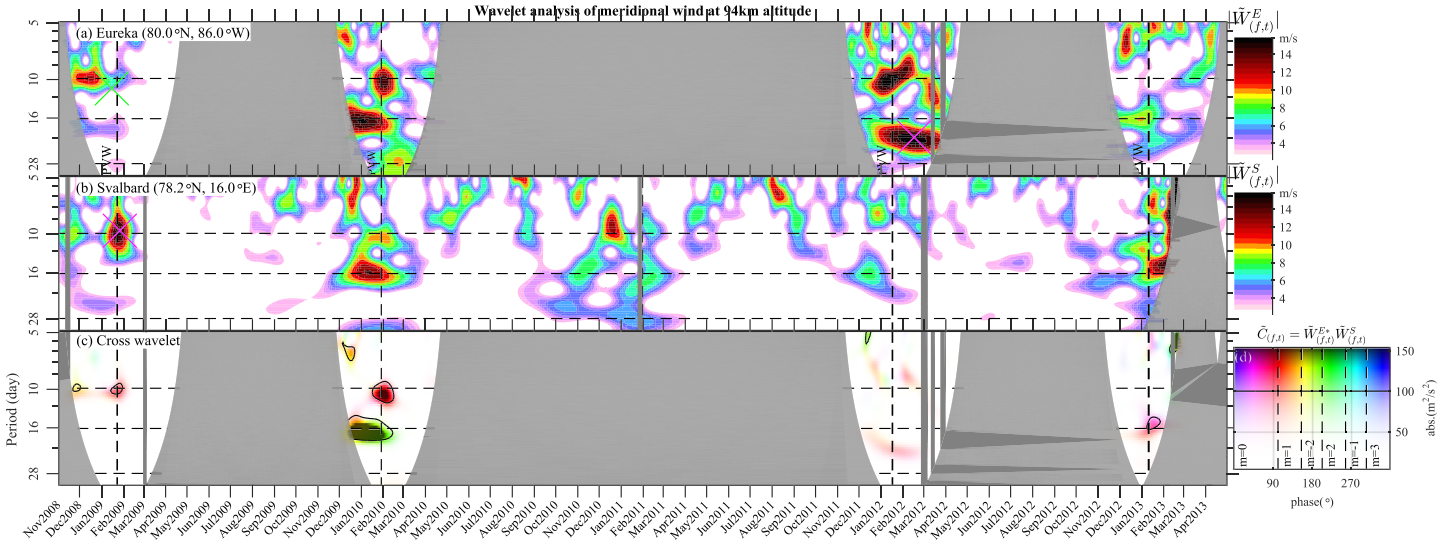

Figure 4. Same plot as Figure 2 but for the meridional component.

$M_c := \{-2, -1, 0, 1, 2, 3\}$ is defined as the maximum set under the constraints of N and m introduced in Appendix A1.

In the wavelet spectrum, $|\tilde{C}_{(f,t)}|$ maximizes at the period 10 days in early 2009 and at 16 days in early 2010, as highlighted by the isoline of $|\tilde{C}_{(f,t)}| = 100\ \mathrm{m}^2/\mathrm{s}^2$. Both maxima occur prior to an SRW onset, represented by the vertical dashed lines in Figure 2c. The phases at both maxima are close to $m = 1$ among $m \in M_c$, which are also the solutions according to the optimization in equation (A3).

3.3. Butterworth Filtering

Figure 3a is a zoomed version of Figure 2c around SSW 2009. For investigating the duration of the 10-day oscillation, the hourly wind is filtered in the period range between 7 and 13 days using a Butterworth filter. The filtered wind, displayed in Figure 3b, illustrates that the near-10-day oscillations exist at both stations with different phases. The oscillation at Svalbard lasts only about three whole periods between 10 December 2008 and 10 January 2009, which suggests the underlying wave is transient.

Similarly, Figure 3c is a zoomed version of Figure 2c around the SSW 2010, and the zonal wind is low-pass filtered with a cutoff period of 10 days and shown in Figure 3d. Instead of the band-pass filter used in Figure 3b, here low-pass Butterworth filter is used because in Figures 2a and 2b there is not any comparable oscillation

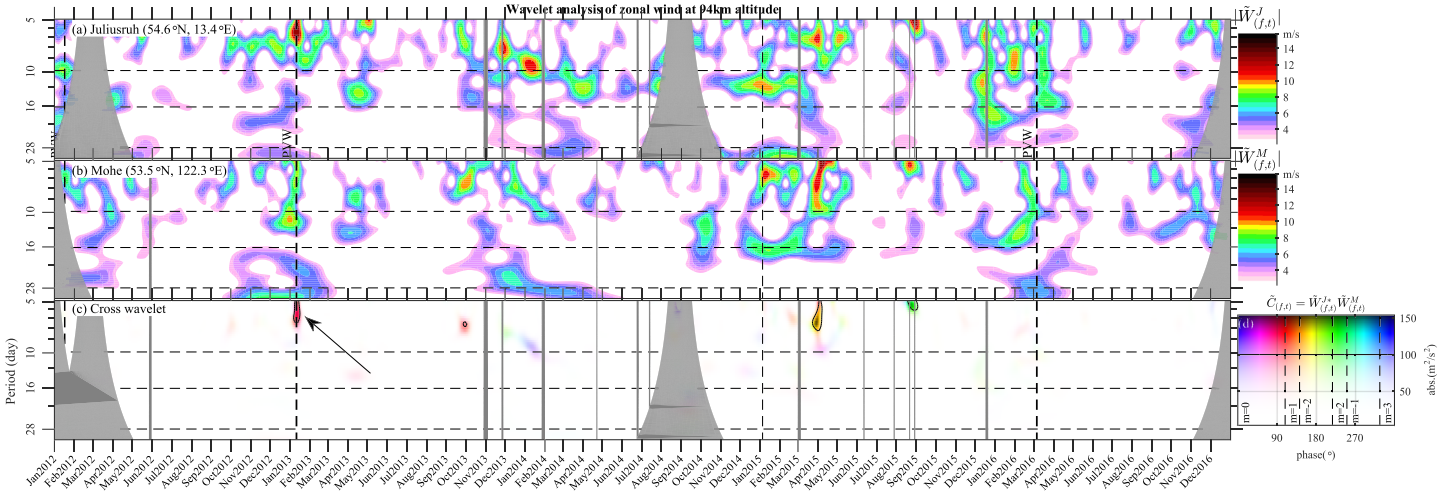

Figure 5. Same plot as Figure 2 but for the radar pair at the middle latitudes.

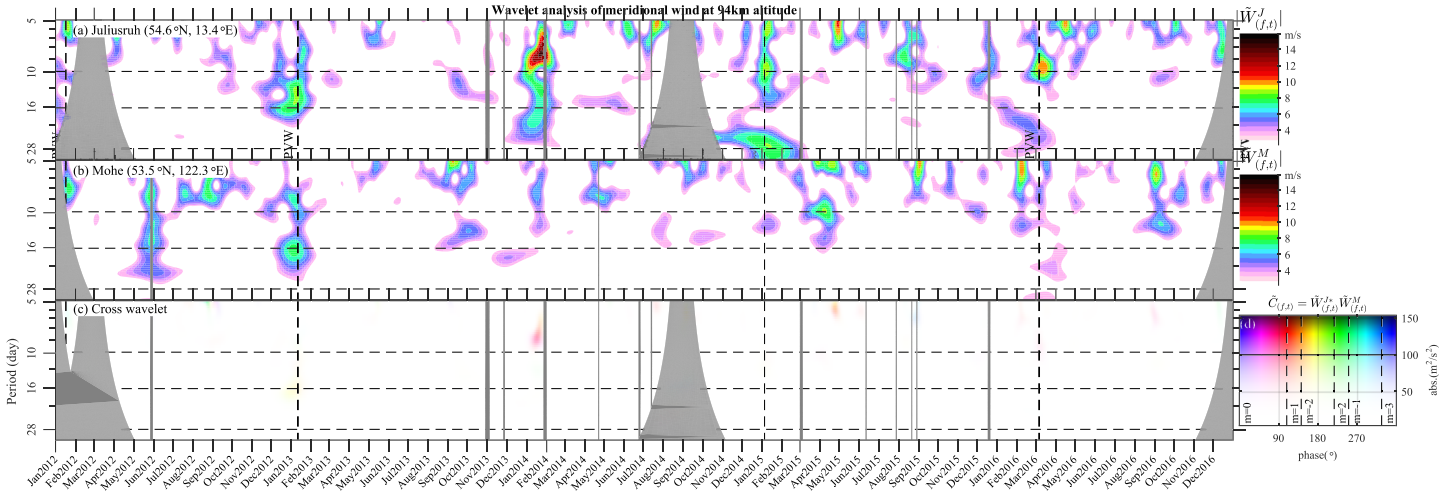

Figure 6. Same plot as Figure 4 but for the radar pair at the middle latitudes.

at lower frequencies. Figure 3d illustrates that the oscillation at Svalbard leads that at Eureka, for example, around the end of December 2009. Such a phase leading lasts from about 5 December 2009 to about 20 January 2010, about three periods of 16-day oscillation, suggesting the underlying wave is also transient.

3.4. Wavelet Spectra of Meridional Wind

Figure 4 displays the same plots as in Figure 2 but for the meridional wind v. At first glance, Figure 4 is similar to Figure 2. The wavelet spectra for the individual radars are populated with significant isolated peaks in the winters, whereas the cross-wavelet is populated with peaks at mostly periods of 10 and 16 days around mostly the onsets, most of which are characterized by $m = 1$ and last for less than 1 month.

Behind the above similarities between u and v there are many differences in the details. In the wavelet spectra, v peaks are in some cases much stronger than the corresponding peaks in u (e.g., at the magenta crosses in Figures 2a, 2b, 4a, and 4b), whereas in some other cases, peaks are much stronger in u (e.g., at the green crosses in Figures 2b and 4b). Not surprisingly, the cross-wavelet spectrum of v in Figure 4c is also not identical to that of u in Figure 2c. At SSW 2009, the peak in v does not occur synchronously with the peak in u but delays about 1 month afterward. At SSW 2010, although the peaks in v and u occur almost at the same time, they are characterized by different wave number, that is, $m = 1$ and 2, respectively.

3.5. At a Middle Latitude

The above sections presented the results at the polar latitude. For comparison, Figures 5 and 6 present the same results as Figures 2 and 4 but for the midlatitude network. Figures 5 and 4 span from 2012 to 2016, overlapping Figures 2 and 4 only for one and a half winters.

In comparison to the spectra at the polar latitude, the amplitudes at the middle latitudes are generally weaker in both the wavelet and cross-wavelet spectra. The wavelet spectral peaks in Figures 5a, 5b, 6a, and 6b occur very rarely above 12 m/s, whereas those in Figures 2a, 2b, 4a, and 4b are often above 16 m/s. In the cross-wavelet spectra in Figures 5c and 6c, no peak occurs at $|\tilde{C}| > 100$ m^2/s^2 along the periods of around 10 or 16 days.

4. Discussions

In the previous section, wavelet analysis, cross-wavelet analysis, and Butterworth filtering are used to explore the mesospheric wind detected at two zonally separated stations at 79°N latitude during four winters. The wavelet analysis presents isolated spectral peaks in both frequency and time. Co-occurring at both stations are peaks at onsets of SSWs. The co-occurrence is quantified by the cross-wavelet spectrum, which allows diagnosing the zonal wave number. The diagnosis results are summarized in Table 1. For a comparison, multiyear observations from a dual-station network at 54°N were also diagnosed. At the middle latitudes, the spectra at periods of 10 and 16 days are weaker than those at the polar latitude. Therefore, below we focus mainly on the polar latitude. Section 4.1 explains the cross-wavelet spectral peaks in terms of RNMs,

Table 1
m Reads From Figures 2 and 4, at $|\tilde{C}| > 100\ m^2/s^2$

Year	SSW type	10 days	16 days
2009	major	$m_u = 1, m_v = 1$	
2010	major	$m_v = 1$	$m_u = 1, m_v = 2$
2012	minor		
2013	major		$m_v = 1$

section 4.2 introduces the potential problems of our approach, and 4.3 discusses the potential association of RNMs with SSWs.

4.1. Zonal Wave Number Evidence for RNMs

In Figures 2c and 4c around the periods of 10 and 16 days, there are six spectral peaks at $|\tilde{C}| > 100$ m^2/s^2. Five of them are associated with m =1, namely, westward traveling zonal wave number 1 structure, and the last one is $m = 2$, as summarized in Table 1. The m =1 peaks suggest that the underlying waves are the RNMs (1, 2) and (1, 3), namely, 10- and 16-day waves (e.g., Forbes, 1995b; Sassi et al., 2012). Also, in the troposphere 16-day wave was observed before SSW 2010 (e.g., Figure 2 in Madden, 2019). Similarly, manifestations of 16-day waves coincided in different atmospheric layers were also reported prior to the onset of SSW 2003/2004 and explained as vertical wave propagation (Pancheva et al., 2008). The 10-day wave during SSW 2009 was reported in space-based observations (Figure 5f in Yamazaki & Matthias, 2019) and in the global meteorological products issued by an Advanced Level Physics High-Altitude (ALPHA) prototype of the Navy Operational Global Atmospheric Prediction System (NOGAPS) (Figure 7e in Sassi et al., 2012). The space-based observations (Yamazaki & Matthias, 2019) also revealed the transiency of the 10-day wave as revealed in Figure 3a. According to the classical theory of normal modes (e.g., Madden, 2007; Yamazaki & Matthias, 2019), the RNMs in the horizontal wind are often not circularly polarized; namely, the amplitudes in u are different from those in v. This difference contributes to the fact that the spectral peaks in Figure 2c do not coincide with those in Figure 4c. The classical theory also illustrates that both 10- and 16-day waves in both u and v are stronger at polar latitudes than those at middle latitudes, which could explain the latitude variations described in the last paragraph of section 3.5. At the middle latitudes, as marked by the black arrow in Figure 5c, a peak occurs along the period 5–7 days around SSW 2013 at $|\tilde{C}| > 100$ m^2/s^2, associated with m =1. Using the same Mohe radar, Gong et al. (2018) detected the periodicity in a single-station analysis and explained it as a signature of RNM (1, 1), namely, the 5-day wave. Here, our diagnosis $m = 1$ supports the occurrence of that RNM. The 5-day wave activity in SSW 2013 was also revealed in satellite observations (Forbes & Zhang, 2017; Yamazaki, 2018).

As an exception with $m \neq 1$, the 16-day oscillation with $m = 2$ at the onset of SSW 2010 in Figure 4c could also be explained as a normal mode, for example, (2, 3) or (2, 4) (e.g., Hirota & Hirooka, 1984; Kasahara, 1980). Another potential possibility accounting for the $m = 2$ sixteen-day oscillation is the wave-wave nonlinear interaction between the 16-day wave and a SRW with $m = 1$. The interaction could generate secondary waves at the period of 16 days with $m = 0$ or $m = 2$, according to the resonance conditions in which wave number m and frequency f of the secondary waves are equal to either the sum or difference of those of the parent waves (e.g., He et al., 2017). The $m = 2$ secondary wave might amplify the above mentioned RNMs (2, 3) or (2, 4) resonantly. Wave-wave interactions occur broadly between global-scale atmospheric waves, for example, tides, RNMs, or SRWs. In terms of these three types, six categories have been studied, that is, tide-tide, RNM-RNM, SRW-SRW, tide-RNM, tide-SRW, and RNM-SRW interactions (e.g., Forbes & Zhang, 2017; He & Chau, 2019; He et al., 2017; Liu et al., 2006; Pancheva et al., 2004; Pedatella & Liu, 2013; Pogoreltsev, 2001). In the RNM-SRW category, to the authors' knowledge, evidence was reported only for the interaction between quasi 2-day wave and SRW (Gu et al., 2015). Our result suggests that 16-day wave could also interact nonlinearly with SRW.

Our m diagnosis also allows distinguishing RNM-associated waves from the multiday disturbances associated with solar rotation. The disturbances are suggested to arise from solar coronal holes associated with emission of the high-speed stream (e.g., Krieger et al., 1973; Temmer et al., 2007). Multiple coronal holes might elongate to lower solar latitudes (e.g., Burlaga et al., 1978) and produce disturbances in solar-terrestrial space environment at harmonics of the solar rotation period, for example, 7, 9, 13.5, and 27 days, as broadly

reported from the solar wind to the ionosphere and thermosphere (e.g., He et al., 2011; Lei et al., 2011). Recently, signatures of such disturbances were also reported in the mesosphere (e.g., von Savigny et al., 2019; Yi et al., 2017). These disturbances are impulsive, recurring every 9, 13.5, or 27 days close to the RNM periods considered here, but they are not free waves and do not propagate evenly on the time scale of these periods.

4.2. Limitations of Our Approach and Their Implications

Our phase differencing approach has some limitations. The first is a limitation of all spectral analysis in which the underlying waves are assumed to be time-invariant on the spectrum-resolved temporal scale. Spectral analyses cannot deal with time-variant waves. For instance, if an enhancing SRW is superposed to an identical SRW but weakening with a different zonal phase, the superposition will be detected as a traveling wave in spectral analyses. Such a superposition of time-variant waves provides a third explanation for the $m = 2$ estimation listed in Table 1 as well as for RNM-like structures observed with a wide range of m (e.g., comparable amplitudes of six wave numbers, $m = \pm 3, \pm 2, \pm 1$, at the period 16 days; cf. John & Kumar, 2016; Kleinknecht et al., 2014; McDonald et al., 2011). Therefore, RNM-like structures with non-RNM m might not be signatures of waves.

The second limitation is that our approach uses only two stations, whereas RNMs are global-scale transverse waves traveling presumptively in the zonal direction. In the real atmosphere, RNMs might be distorted and not travel exactly zonally and therefor pass only one station but miss the other. This limitation implicates that our cross-wavelet spectra might not completely capture all RNM signatures. The wavelet spectral peaks occurring at only one station might also be signatures of RNMs. For example, in Figures 2b, 5a, and 5b, there are many peaks at the period 20–33 days, which are potentially signatures of the RNM (1, 4), namely, the 25-day wave (cf. Sassi et al., 2012), although our approach failed in identifying their wave number. In comparison with 5-, 10-, or 16-day waves, the 25-day wave has attracted less interest (e.g., Branstator, 1987; Kushnir, 1987; Zhao et al., 2019).

4.3. Association Between RNMs and SSWs

Although SRWs are well known for triggering SSWs (e.g., Matsuno, 1971), there is no consensus on the relations between RNMs and SSWs. Sassi et al. (2012) found no evidence to associate RNMs with SSW in their analysis of NOGAPS-ALPHA products for the boreal winters of 2005, 2006, 2008, and 2009. On the contrary, the more popular opinion is that there are associations between RNMs and SSWs: RNMs occur either before or after the SSW onsets. Pancheva et al. (2008) found that during SSW 2003–2004, the MLT was dominated by the 16-day wave before the onset but by waves at longer periods after the onset, through analyzing observations from eight radar stations, UKMO assimilated winds, and SABER temperatures. However, Stray et al. (2015) reported that it is after, rather than before, the onset when mesospheric RW-like oscillations with zonal wave number 1 structure were enhanced, in a statistic study of seven SSWs between 2000 and 2008 using on meridian meteor winds from eight SuperDARN radars. Recently, Yamazaki and Matthias (2019) noted that the relationship between RNMs and SSW depends on the seasonal timing of the SSW using measurements from the Aura MLS during 2004–2018.

The four winters explored in Figures 2 and 4 comprise four SSWs (see Table 1) among which SSW 2012 is minor while the other three are major (e.g., Butler et al., 2015). All the major SSWs are accompanied by at least one predominant RNM signature in our wave number diagnosis, and all of the predominant RNM signatures occurred in the major SSWs. Therefore, our results suggest that there is an association between RNMs and major SSWs. However, in Table 1 the occurrences of the 10- and 16-day waves are different from one SSW to another. We argue that to investigate the year-to-year variability of the occurrences entails more SSWs. After SSW onsets, peaks around 10, 16, and 28 days often occur in the individual wavelet spectra (Figures 2a, 2b, 4a, and 4b), but not in the cross-wavelet spectra (Figures 2c and 4c). These oscillations might also be signatures of RNMs as discussed in section 4.2. RNM-like waves have been observed after the onsets of SSWs 2006 and 2012 (e.g., Chandran et al., 2013; Manney et al., 2008; Siskind et al., 2010) and were termed as "secondary waves" to be distinguished from those existing prior to SSWs. The secondary RNMs were suggested to arise locally in the mesosphere (e.g., Chandran et al., 2013), unlike RNMs existing prior to SSWs which occur in both the stratosphere and mesosphere (e.g., Pancheva et al., 2008). The underlying mechanism is still under debate. Potential hypotheses include zonally asymmetric gravity wave breaking (Manney et al., 2008), a combination of forcing from below and in situ instability near the stratopause (Siskind et al., 2010), and planetary wave amplification by stimulated tidal decay (PASTIDE

He et al., 2017). In PASTIDE, solar migrating semidiurnal tide transport energy to RNMs by nonlinear interaction with RNMs.

5. Summary

Mesospheric wind detected by two zonally separated radars at about 79°N latitude between 2009 and 2013 is used to explore RNMs through PDT. Wavelet spectra of the wind illustrate that oscillations at the periods of 10 and 16 days often occur in winters. Butterworth filtering demonstrates that the oscillations last for a few whole-circle periods. The six most significant oscillations occur around onsets of SSWs 2009, 2010, and 2013. The phase difference analysis suggests that five of the six are characterized by $m = 1$ (westward traveling zonal wave number 1), whereas the sixth is characterized by $m = 2$. We explain the $m = 1$ oscillations as signatures of the RNMs, 10- and 16-day waves, and discuss three possibilities for the $m = 2$. The possibilities are (1) a normal mode, (2) secondary waves of nonlinear interactions of RNMs and SRW, and (3) mixing or transition of multi waves. In addition, we also explored similar observations between 2012 and 2016 collected by two radars at about 54°N for comparison. Signatures of 10- and 16-day waves at 54°N are significantly weaker than those at 79°N. At 54°N, a significant spectral peak at the period of 5–7 days occurs at the onset of SSW 2013. Our diagnoses illustrate the peak associated with m =1, suggesting the underlying wave is the RNM, 5-day wave. The occurrences of the above RNMs suggest associations between RNMs and SSWs.

Appendix A: Phase Differencing Technique

A zonally propagating wave at frequency $f = \omega/2\pi$ and zonal wave number m could be represented as $\tilde{u}(\lambda, t) = \tilde{u}_0 e^{i(\omega t + m\lambda)}$, where λ denotes the longitude. For two longitude λ_1 and λ_2, there is a time-independent function,

$$\tilde{p}(\lambda_1, \lambda_2) := \tilde{u}^*(\lambda_1, t)\tilde{u}(\lambda_2, t) = |\tilde{u}_0|^2 e^{im(\lambda_2 - \lambda_1)} \tag{A1}$$

Here, $\tilde{u}^*$ represents the complex conjugate of $\tilde{u}$. Therefore,

$$\arg\{\tilde{p}\} + 2N\pi = m(\lambda_2 - \lambda_1) \tag{A2}$$

Here, $\arg\{\tilde{p}\}$ in the range from $-\pi$ to π excluding $-\pi$ itself denotes the argument of $\tilde{p}$, and $N \in \mathbb{Z}$ is an integer, representing the whole-cycle ambiguity. Assume $\tilde{p}$ has an observational estimation $\hat{\tilde{p}}$. Then, under some constraints of N and potentially m, m could be determined through an optimization,

$$\hat{m} = \underset{N,m}{\operatorname{argmin}} \left| \arg\left\{\hat{\tilde{p}}\right\} + 2N\pi - m(\lambda_2 - \lambda_1) \right| \tag{A3}$$

To estimate $\tilde{p}$ observationally entails the so-called single-wave assumption, namely, only one wave exists within the resolved ranges of frequency and time. Under this assumption, $\tilde{p}$ could be estimated through spectral analyses (e.g., cross-wavelet analysis and least squares spectral analysis, respectively He, Chau, Hall, et al., 2018, 2020). The current work uses cross-wavelet analyses (e.g., Grinsted et al., 2004; He, Chau, Stober, et al., 2018). Besides, to deal with the whole-cycle ambiguity in the optimization of equation (A3), a constraint $N = 0$ was broadly used, either specified explicitly (e.g., Walker et al., 2004) or used implicitly (e.g., Pancheva et al., 2008). The constraint implies that the underlying wave's wavelength is assumed to be longer than twice the radar spacing and therefore was called the long-wave assumption. The $N = 0$ constraint could be relaxed, for example, according to prior knowledge about the underlying waves (e.g., He, Chau, Stober, et al., 2018) or using additional stations (e.g., He et al., 2020). For instance, He, Chau, Stober, et al. (2018) relaxed $N = 0$ to $N \in \{-1, 0, 1\}$ by implementing a second constraint that $m \in \mathbb{Z}$ is an integer according to prior knowledge. Similarly, in diagnosing RW-like oscillations, the current study uses the constraints of $N \in \{-1, 0, 1\}$ and $m \in \mathbb{Z}$ according to the prior knowledge from existing publications on RWs (e.g., Kleinknecht et al., 2014; Madden, 2007; Sassi et al., 2012).

Visualizations of the optimization of equation (A3) could be found in Figure 2 in He, Chau, Stober, et al. (2018) and Figure 3 in He, Chau, Hall, et al. (2018). These figures present the visualizations in complex planes, in which one radial solid line denotes the phase difference $m(\lambda_2 - \lambda_1)$ associated with one candidate of m, while each arrow denotes one $\hat{\tilde{p}}$. The task of the optimization is, for each arrow, to search a line from

the m candidates so that the cross angle between the arrow and the line minimizes. Readers are referred to the relevant discussions in He, Chau, Stober, et al. (2018) and He, Chau, Hall, et al. (2018) for details.

Acknowledgments
The authors appreciate Alan Manson (alan.manson@usask.ca) and Chris Meek (chris.meek@usask.ca) for providing the observations at Eureka and their discussions in the contents of Manson et al. (2009). Maosheng He appreciates Jeffrey M. Forbes for proposing the nonlinear interaction between the 16-day wave and an SRW in explaining the $m = 2$ structure. This work was supported by Leibniz-Gemeinschaft under WATILA project (SAW-2-15-IAP-5 383) and Deutsche Forschungsgemeinschaft (DFG, German Research Foundation) under SPP 1788 (DynamicEarth) projects CH1482/1-2 (DYNAMITE-2). Yosuke Yamazaki was partially supported by the Deutsche Forschungsgemeinschaft (DFG) Grant YA-574-3-1. The raw data could be requested from Alan Manson for Eureka, and Chris M. Hall (chris.hall@uit.no) and Masaki Tsutsumi (tutumi@nipr.ac.jp) for Svalbard. The Eureka radar is operated by PEARL (Polar Environment Atmospheric Research Laboratory), a facility of CANDAC (Canadian Network for the Detection of Atmospheric Change). The data from Mohe are provided by the Data Center for Geophysics (http://wdc.geophys.ac.cn/), National Earth System Science Data Sharing Infrastructure at BNOSE (Beijing National Observatory of Space Environment), IGGCAS (Institute of Geology and Geophysics, Chinese Academy of Sciences). The postprocessed data in this paper are available at the Harvard Dataverse (through https://doi.org/10.7910/DVN/HZ1ZFB).

References

Allison, M. (1990). Planetary waves in Jupiter's equatorial atmosphere. *Icarus*, *83*(2), 282–307. https://doi.org/10.1016/0019-1035(90)90069-L

Branstator, G. (1987). A striking example of the atmosphere's leading traveling pattern. https://doi.org/10.1175/1520-0469(1987)044h2310:aseotai2.0.co;2

Burlaga, L. F., Behannon, K. W., Hansen, S. F., Pneuman, G. W., & Feldman, W. C. (1978). Sources of magnetic fields in recurrent interplanetary streams. *Journal of Geophysical Research*, *83*(A9), 4177–4185. https://doi.org/10.1029/JA083iA09p04177

Butler, A. H., Seidel, D. J., Hardiman, S. C., Butchart, N., Birner, T., & Match, A. (2015). Defining sudden stratospheric warmings. *Bulletin of the American Meteorological Society*, *96*(11), 1913–1928. https://doi.org/10.1175/BAMS-D-13-00173.1

Chandran, A., Garcia, R. R., Collins, R. L., & Chang, L. C. (2013). Secondary planetary waves in the middle and upper atmosphere following the stratospheric sudden warming event of January 2012. *Geophysical Research Letters*, *40*, 1861–1867. https://doi.org/10.1002/grl.50373

Clark, R. R., Burrage, M. D., Franke, S. J., Manson, A. H., Meek, C. E., Mitchell, N. J., & Muller, H. G. (2002). Observations of 7-D planetary waves with MLT radars and the UARS-HRDI instrument. *Journal of Atmospheric and Solar-Terrestrial Physics*, *64*(8), 1217–1228. https://doi.org/10.1016/S1364-6826(02)00070-6

Elhawary, R., & Forbes, J. M. (2016). Planetary wave variability of Sq currents. *Journal of Geophysical Research: Space Physics*, *121*, 11,316–11,332. https://doi.org/10.1002/2016JA023242

Fedulina, I. N. N., Pogoreltsev, A. I. I., Vaughan, G., Pogoreltsev, A. I., Vaughan, G., Pogoreltsev, A. I. I., & Vaughan, G. (2004). Seasonal, interannual and short-term variability of planetary waves in Met Office stratospheric assimilated fields. *Quarterly Journal of the Royal Meteorological Society*, *130*(602 PART A), 2445–2458. https://doi.org/10.1256/qj.02.200

Forbes, J. M. (1995a). Quasi 16-day oscillation in the mesosphere and lower thermosphere. *Journal of Geophysical Research*, *100*(D5), 9149–9163. https://doi.org/10.1029/94JD02157

Forbes, J. M. (1995b). Tidal and planetary waves. *Geophysical Monograph Series*, *87*, 67–87. https://doi.org/10.1029/GM087p0067

Forbes, J. M., & Zhang, X. (2015). Quasi-10-day wave in the atmosphere. *Journal of Geophysical Research: Atmospheres*, *120*, 11,079–11,089. https://doi.org/10.1002/2015JD023327

Forbes, J. M., & Zhang, X. (2017). The quasi-6 day wave and its interactions with solar tides. *Journal of Geophysical Research: Space Physics*, *122*, 4764–4776. https://doi.org/10.1002/2017JA023954

Gong, Y., Li, C., Ma, Z., Zhang, S., Zhou, Q., Huang, C., et al. (2018). Study of the quasi-5-day wave in the MLT region by a meteor radar chain. *Journal of Geophysical Research: Atmospheres*, *123*, 9474–9487. https://doi.org/10.1029/2018JD029355

Grinsted, A., Moore, J. C., & Jevrejeva, S. (2004). Application of the cross wavelet transform and wavelet coherence to geophysical time series. *Nonlinear Processes in Geophysics*, *11*(5/6), 561–566. https://doi.org/10.5194/npg-11-561-2004

Grossmann, A., Kronland-Martinet, R., & Morlet, J. (1990). Reading and understanding continuous wavelet transforms. In J.-M. Combes, A. Grossmann, & P. Tchamitchian (Eds.), *Wavelets* (pp. 2–20). Berlin, Heidelberg: Springer Berlin Heidelberg.

Gu, S. Y., Liu, H. L., Li, T., Dou, X., Wu, Q., & Russell, J. M. (2015). Evidence of nonlinear interaction between quasi 2 day wave and quasi-stationary wave. *Journal of Geophysical Research: Space Physics*, *120*, 1256–1263. https://doi.org/10.1002/2014JA020919

Hall, C. M., Aso, T., & Tsutsumi, M. (2002). An examination of high latitude upper mesosphere dynamic stability using the Nippon/Norway Svalbard Meteor Radar. *Geophysical Research Letters*, *29*(8), 121–1–121–3. https://doi.org/10.1029/2001gl014229

He, M., & Chau, J. L. (2019). Mesospheric semidiurnal tides and near-12 h waves through jointly analyzing observations of five specular meteor radars from three longitudinal sectors at boreal midlatitudes. *Atmospheric Chemistry and Physics*, *19*(9), 5993–6006. https://doi.org/10.5194/acp-19-5993-2019

He, M., Chau, J. L., Hall, C. M., Tsutsumi, M., Meek, C., & Hoffmann, P. (2018). The 16-day planetary wave triggers the SW1-tidal-like signatures during 2009 sudden stratospheric warming. *Geophysical Research Letters*, *45*, 12,631–12,638. https://doi.org/10.1029/2018GL079798

He, M., Chau, J. L., Stober, G., Hall, C. M., Tsutsumi, M., & Hoffmann, P. (2017). Application of Manley-Rowe relation in analyzing nonlinear interactions between planetary waves and the solar semidiurnal tide during 2009 sudden stratospheric warming event. *Journal of Geophysical Research: Space Physics*, *122*, 10,783–10,795. https://doi.org/10.1002/2017JA024630

He, M., Chau, J. L., Stober, G., Li, G., Ning, B., & Hoffmann, P. (2018). Relations between semidiurnal tidal variants through diagnosing the zonal wavenumber using a phase differencing technique based on two ground-based detectors. *Journal of Geophysical Research: Atmosheres*, *123*, 4015–4026. https://doi.org/10.1002/2018JD028400

He, M., Forbes, J. M., Chau, J. L., Li, G., Wan, W., & Korotyshkin, D. V. (2020). High-order solar migrating tides quench at SSW onsets. *Geophysical Research Letters*, *47*, e2019GL086778. https://doi.org/10.1029/2019GL086778

He, M., Liu, L., Wan, W., & Zhao, B. (2011). A study on the nighttime midlatitude ionospheric trough. *Journal of Geophysical Research*, *116*, A05315. https://doi.org/10.1029/2010JA016252

Hirota, I., & Hirooka, T. (1984). Normal mode Rossby waves observed in the upper stratosphere. Part II: Second antisymmetric and symmetric modes of zonal wavenumbers 1 and 2. *Journal of the Atmospheric Sciences*, *42*(6), 536–548. https://doi.org/10.1175/1520-0469(1985)042%3C0536:NMRWOI%3E2.0.CO;2

Holton, J. R., & Hakim, G. J. (2013). Chapter 5—Atmospheric oscillations: Linear perturbation theory, (Fifth Edit). In J. R. Holton, & G. J. Hakim (Eds.), *An introduction to dynamic meteorology* (pp. 127–170). Boston: Academic Press. https://doi.org/10.1016/B978-0-12-384866-6.00005-2

Jiang, G., Xu, J., Xiong, J., Ma, R., Ning, B., Murayama, Y., et al. (2008). A case study of the mesospheric 6.5-day wave observed by radar systems. *Journal of Geophysical Research*, *113*, D16111. https://doi.org/10.1029/2008JD009907

John, S. R., & Kumar, K. K. (2016). Global normal mode planetary wave activity: A study using TIMED/SABER observations from the stratosphere to the mesosphere-lower thermosphere. *Climate Dynamics*, *47*(12), 3863–3881. https://doi.org/10.1007/s00382-016-3046-2

Kasahara, A. (1980). Effect of zonal flows on the free oscillations of a barotropic atmosphere. *Journal of the Atmospheric Sciences*, *37*(5), 917–929. https://doi.org/10.1175/1520-0469(1980)037%3C0917:EOZFOT%3E2.0.CO;2

Kleinknecht, N. H., Espy, P. J., & Hibbins, R. E. (2014). The climatology of zonal wave numbers 1 and 2 planetary wave structure in the MLT using a chain of Northern Hemisphere SuperDARN radars. *Journal of Geophysical Research: Atmospheres*, *119*, 1292–1307. https://doi.org/10.1002/2013JD019850

Krieger, A. S., Timothy, A. F., & Roelof, E. C. (1973). A coronal hole and its identification as the source of a high velocity solar wind stream. *Solar Physics*, *29*(2), 505–525. https://doi.org/10.1007/BF00150828

Kushnir, Y. (1987). Retrograding wintertime low-frequency disturbances over the North Pacific Ocean. https://doi.org/10.1175/1520-0469(1987)044<2727:rwlfdo>2.0.co;2

Lei, J., Thayer, J. P., Wang, W., & McPherron, R. L. (2011). Impact of CIR storms on thermosphere density variability during the solar minimum of 2008. *Solar Physics*, *274*(1-2), 427–437. https://doi.org/10.1007/s11207-010-9563-y

Liu, R., Lu, D., Yi, F., & Hu, X. (2006). Quadratic nonlinear interactions between atmospheric tides in the mid-latitude winter lower thermosphere. *Journal of Atmospheric and Solar-Terrestrial Physics*, *68*(11), 1245–1259. https://doi.org/10.1016/j.jastp.2006.03.004

Longuet-Higgins, M. S. (1968). The Eigenfunctions of Laplace's tidal equations over a sphere. *Philosophical Transactions of the Royal Society A*, *262*(1132), 511–607. https://doi.org/10.1098/rsta.1968.0003

Lovelace, R. V. E., Li, H., Colgate, S. A., & Nelson, A. F. (1999). Rossby wave instability of Keplerian accretion disks. *The Astrophysical Journal*, *513*(2), 805–810. https://doi.org/10.1086/306900

Madden, R. A. (1979). Observations of large-scale traveling Rossby waves. *Reviews of Geophysics*, *17*(8), 1935–1949. https://doi.org/10.1029/RG017i008p01935

Madden, R. A. (2007). Large-scale, free Rossby waves in the atmosphere—An update. *Tellus A: Dynamic Meteorology and Oceanography*, *59*(5), 571–590. https://doi.org/10.1111/j.1600-0870.2007.00257.x

Madden, R. A. (2019). How I learned to love normal-mode Rossby-Haurwitz waves. *Bulletin of the American Meteorological Society*, *100*(3), 503–511. https://doi.org/10.1175/BAMS-D-17-0293.1

Manney, G. L., Krüger, K., Pawson, S., Minschwaner, K., Schwartz, M. J., Daffer, W. H., et al. (2008). The evolution of the stratopause during the 2006 major warming: Satellite data and assimilated meteorological analyses. *Journal of Geophysical Research*, *113*, D11115. https://doi.org/10.1029/2007JD09097

Manson, A. H., Meek, C. E., Chshyolkova, T., Xu, X., Aso, T., Drummond, J. R., et al. (2009). Arctic tidal characteristics at Eureka (80 N, 86 W) and Svalbard (78 N, 16E) for 2006/07: Seasonal and longitudinal variations, migrating and non-migrating tides. *Annales Geophysicae*, *27*(3), 1153–1173. https://doi.org/10.5194/angeo-27-1153-2009

Matsuno, T. (1971). A dynamical model of the stratospheric sudden warming. *Journal of the Atmospheric Sciences*, *28*(8), 1479–1494. https://doi.org/10.1175/1520-0469(1971)028<1479:ADMOTS>2.0.CO;2

McDonald, A. J., Hibbins, R. E., & Jarvis, M. J. (2011). Properties of the quasi 16 day wave derived from EOS MLS observations. *Journal of Geophysical Research*, *116*, D06112. https://doi.org/10.1029/2010JD014719

McIntosh, S. W., Cramer, W. J., Pichardo Marcano, M., & Leamon, R. J. (2017). The detection of Rossby-like waves on the Sun. *Nature Astronomy*, *1*, 1–5. https://doi.org/10.1038/s41550-017-0086

Melde, F. (1860). Ueber die Erregung stehender Wellen eines fadenförmigen Körpers. *Annals of Physics*, *187*(12), 513–537. https://doi.org/10.1002/andp.18601871202

Murphy, D. J. (2003). Observations of a nonmigrating component of the semidiurnal tide over Antarctica. *Journal of Geophysical Research*, *108*(D8), 4241. https://doi.org/10.1029/2002JD003077

Pancheva, D., Mitchell, N. J., Manson, A. H., Meek, C. E., Jacobi, C., Portnyagin, Y., et al. (2004). Variability of the quasi-2-day wave observed in the MLT region during the PSMOS campaign of June–August 1999. *Journal of Atmospheric and Solar-Terrestrial Physics*, *66*(6-9), 539–565. https://doi.org/10.1016/j.jastp.2004.01.008

Pancheva, D., Mukhtarov, P., Mitchell, N. J., Merzlyakov, E., Smith, A. K., Andonov, B., et al. (2008). Planetary waves in coupling the stratosphere and mesosphere during the major stratospheric warming in 2003/2004. *Journal of Geophysical Research*, *113*, D12105. https://doi.org/10.1029/2007JD009011

Pedatella, N. M., & Liu, H. L. (2013). The influence of atmospheric tide and planetary wave variability during sudden stratosphere warmings on the low latitude ionosphere. *Journal of Geophysical Research: Space Physics*, *118*, 5333–5347. https://doi.org/10.1002/jgra.50492

Pogoreltsev, A. I. (2001). Numerical simulation of secondary planetary waves arising from the nonlinear interaction of the normal atmospheric modes. *Physics and Chemistry of the Earth, Part C: Solar, Terrestrial & Planetary Science*, *26*(6), 395–403. https://doi.org/10.1016/S1464-1917(01)00020-4

Pogoreltsev, A. I., Pancheva, D., & Mitchell, N. J. (2002). Secondary planetary waves in the middle atmosphere: Numerical simulation and analysis of the neutral wind data. *Journal of Atmospheric and Solar-Terrestrial Physics*, *64*(8-11), 1251–1261. https://doi.org/10.1016/S1364-6826(02)00039-1

Read, P. L., Dowling, T. E., & Schubert, G. (2009). Saturn's rotation period from its atmospheric planetary-wave configuration. *Nature*, *460*(7255), 608–610. https://doi.org/10.1038/nature08194

Reed, R. (1963). On the cause of the stratospheric sudden warming phenomenon. *Meteorology Abhand*, *36*, 315–334.

Rossby, C.-G. (1939). Relation between variations in the intensity of the zonal circulation of the atmosphere and the displacements of the semi-permanent centers of action. *Journal of Marine Research*, *2*(1), 38–55. https://doi.org/10.1357/002224039806649023

Salby, M. L. (1982a). Sampling theory for asynoptic satellite observations. Part I: Space-time spectra, resolution, and aliasing. *Journal of the Atmospheric Sciences*, *39*(11), 2577–2600. https://doi.org/10.1175/1520-0469(1982)039<2601:stfaso>2.0.co;2

Salby, M. L. (1982b). Sampling theory for asynoptic satellite observations. Part II: Fast Fourier synoptic mapping. *Journal of the Atmospheric Sciences*, *39*(11), 2601–2614. https://doi.org/10.1175/1520-0469(1982)039<2577:STFASO>2.0.CO;2

Salby, M. L. (1984). Survey of planetary-scale traveling waves: The state of theory and observations. *Reviews of Geophysics*, *22*(2), 209–236. https://doi.org/10.1029/RG022i002p00209

Sassi, F., Garcia, R. R., & Hoppel, K. W. (2012). Large-scale Rossby normal modes during some recent Northern Hemisphere winters. *Journal of the Atmospheric Sciences*, *69*(3), 820–839. https://doi.org/10.1175/jas-d-11-0103.1

Siddiqui, T. A., Stolle, C., Luehr, H., & Matzka, J. (2015). On the relationship between weakening of the northern polar vortex and the lunar tidal amplification in the equatorial electrojet. *Journal of Geophysical Research: Space Physics*, *120*, 10,006–10,019. https://doi.org/10.1002/2015JA021683

Singer, W., Hoffmann, P., Kishore Kumar, G., Mitchell, N. J., & Matthias, V. (2013). Atmospheric coupling by gravity waves: Climatology of gravity wave activity, mesospheric turbulence and their relations to solar activity. In F.-J. Lübken (Ed.), *Climate and weather of the Sun-Earth system. Highlights from a priority program* (pp. 409–427). Dordrecht: Springer Netherlands. https://doi.org/10.1007/978-94-007-4348-9_22

Siskind, D. E., Eckermann, S. D., McCormack, J. P., Coy, L., Hoppel, K. W., & Baker, N. L. (2010). Case studies of the mesospheric response to recent minor, major, and extended stratospheric warmings. *Journal of Geophysical Research*, *115*, D00N03. https://doi.org/10.1029/2010JD014114

Smith, A. K. (1985). Wave transience and wave-mean flow interaction caused by the interference of stationary and traveling waves. https://doi.org/10.1175/1520-0469(1985)042<0529:WTAWMF>2.0.CO;2

Stray, N. H., Orsolini, Y. J., Espy, P. J., Limpasuvan, V., & Hibbins, R. E. (2015). Observations of planetary waves in the mesosphere-lower thermosphere during stratospheric warming events. *Atmospheric Chemistry and Physics*, *15*(9), 4997–5005. https://doi.org/10.5194/acp-15-4997-2015

Tajima, T., & Nakamura, T. (2005). Experiments to study the beta-effect in atmospheric dynamics. *Experiments in Fluids*, *39*(3), 621–627. https://doi.org/10.1007/s00348-005-1007-3

Temmer, M., Vrsnak, B., & Veronig, A. M. (2007). Periodic appearance of coronal holes and the related variation of solar wind parameters. *Solar Physics*, *241*(2), 371–383. https://doi.org/10.1007/s11207-007-0336-1

Tung, K. K., & Lindzen, R. S. (1979). A theory of stationary long waves. Part I: A simple theory of blocking. *Monthly Weather Review*, *107*(6), 714–734. https://doi.org/10.1175/1520-0493(1979)107<0714:atoslw>2.0.co;2

von Savigny, C., Peters, D. H. W., & Entzian, G. (2019). Solar 27-day signatures in standard phase height measurements above central Europe. *Atmospheric Chemistry and Physics*, *19*(3), 2079–2093. https://doi.org/10.5194/acp-19-2079-2019

Walker, S. N., Sahraoui, F., Balikhin, M. A., Belmont, G., Pinçon, J. L., Rezeau, L., et al. (2004). A comparison of wave mode identification techniques. *Annales Geophysicae*, *22*(8), 3021–3032. https://doi.org/10.5194/angeo-22-3021-2004

Weber, R. O., & Madden, R. A. (1993). Evidence of traveling external Rossby waves in the ECMWF analyses. *Journal of the Atmospheric Sciences*, *50*(17), 2994–3007. https://doi.org/10.1175/1520-0469(1993)050<2994:eoterw>2.0.co;2

Yamazaki, Y. (2018). Quasi-6-day wave effects on the equatorial ionization anomaly over a solar cycle. *Journal of Geophysical Research: Space Physics*, *123*, 9881–9892. https://doi.org/10.1029/2018JA026014

Yamazaki, Y., & Matthias, V. (2019). Large amplitude quasi-10-day waves in the middle atmosphere during final warmings. *Journal of Geophysical Research: Atmospheres*, *124*, 9874–9892. https://doi.org/10.1029/2019JD030634

Yi, W., Reid, I. M., Xue, X., Younger, J. P., Murphy, D. J., Chen, T., & Dou, X. (2017). Response of neutral mesospheric density to geomagnetic forcing. *Geophysical Research Letters*, *44*, 8647–8655. https://doi.wiley.com/10.1002/2017GL074813

Yu, Y., Wan, W., Ning, B., Liu, L., Wang, Z., Hu, L., & Ren, Z. (2013). Tidal wind mapping from observations of a meteor radar chain in December 2011. *Journal of Geophysical Research: Space Physics*, *118*, 2321–2332. https://doi.org/10.1029/2012JA017976

Zhang, X., & Forbes, J. M. (2014). Lunar tide in the thermosphere and weakening of the northern polar vortex. *Geophysical Research Letters*, *41*, 8201–8207. https://doi.org/10.1002/2014GL062103

Zhao, Y., Taylor, M. J., Pautet, P.-D., Moffat-Griffin, T., Hervig, M. E., Murphy, D. J., et al. (2019). Investigating an unusually large 28-day oscillation in mesospheric temperature over Antarctica using ground-based and satellite measurements. *Journal of Geophysical Research: Atmospheres*, *124*, 8576–8593. https://doi.org/10.1029/2019JD030286